Multi Higgs production via photon fusion at future multi-TeV muon colliders

Mauro Chiesa*
Dipartimento di Fisica, Università di Pavia, and INFN, Sezione di Pavia, Via A. Bassi 6, 27100 Pavia, Italy

Barbara Mele†
INFN, Sezione di Roma, c/o Dipartimento di Fisica, "Sapienza" Università di Roma, P.le Aldo Moro 2, I-00185 Rome, Italy

Fulvio Piccinini‡
INFN, Sezione di Pavia, Via A. Bassi 6, 27100 Pavia, Italy

(Dated: September 22, 2021)

Multi-TeV muon colliders promise an unprecedented potential for exploring the particle-physics energy frontier, and, at the same time, can probe with fantastic accuracy the precise structure of the Standard Model, and in particular of the Higgs boson sector. Here we consider the possibility to measure the loop-suppressed single-, double-, triple-Higgs boson production mediated by the collinear-photon scattering in the channels $\mu^+\mu^- \to \mu^+\mu^-\gamma^*\gamma^* \to \mu^+\mu^- [H, HH, HHH]$. We study total rates and kinematical distributions in the Standard Model, and compare them with the corresponding vector-boson-fusion processes $V^*V^* \to H, HH, HHH$ at muon collisions center-of-mass energies 1.5 TeV $\lesssim \sqrt{s} \lesssim$ 100 TeV. Possible strategies for enhancing the $\gamma\gamma \to H, HH, HHH$ signal over the dominant vector-boson-fusion production are proposed. The sensitivity of total rates to possible anomalies in the Higgs-boson self-couplings is also discussed.

I. INTRODUCTION

The planning of future colliders able to extend the LHC potential of clarifying the origin of the Standard Model (SM) present limitations has recently revived the interest into a multi-TeV muon collider programme [1–10]. The fantastic advantages of using colliding beams made up of muons, that is point-like particles, dramatically less radiating than electrons in a circular collider, face at the moment the difficulties of realising high intensity, low emittance muon beams which are originating from mesons decays via a proton driver [11–15]. Recent progresses [16–19] as well as possible alternatives methods to realize high intensity muon beams [20–22] might overcome in the next few years the present limitations.

Multi-TeV muon colliders could then provide a possible new path to expand the energy frontier in accelerator physics, potentially allowing the direct production of new heavy states, even beyond the reach of alternative future high-energy colliders possibly following LHC [1, 23–25]. Many possible phenomenological implications for beyond-SM searches have recently been considered for multi-TeV muon colliders in [26–43]. At the same time, multi-TeV muon collisions can offer a brand new laboratory to test with high precision the SM predictions for processes involving high-momentum transfer [44, 45]. This holds true especially for the electroweak (EW) sector of the SM whose phenomenology is moderately affected by QCD backgrounds at lepton colliders [46]. In particular, Higgs boson physics can be tested in new energy regimes [23, 45, 47, 48] with the enhancement of extremely challenging production channels like the triple Higgs production which is sensitive to the quartic Higgs self-coupling [49] .

Benefitting from the multi-TeV regime, here we want to analyse the multiple Higgs-boson production initiated by collinear (almost-on-shell) photons radiated by the initial muon beams, and mediated by loops of heavy particles

$$\mu^+\mu^- \to \mu^+\mu^-\gamma^*\gamma^* \to \mu^+\mu^-(n\,H)\,. \tag{1}$$

In particular, we consider the production of one, two and three Higgs bosons in the channels

$$\mu^+\mu^- \to \mu^+\mu^-\,H\,, \tag{2}$$
$$\mu^+\mu^- \to \mu^+\mu^-\,HH\,, \tag{3}$$
$$\mu^+\mu^- \to \mu^+\mu^-\,HHH\,, \tag{4}$$

mediated by the amplitudes $\gamma^*\gamma^* \to H, HH, HHH$, respectively, proceeding via W-boson and top-quark loops. We show in Figures 1 and 2 the Feynman diagrams of the amplitudes $\gamma\gamma \to H, HH$, respectively, and, in Figures 3, a few representative Feynman diagrams of the amplitude $\gamma\gamma \to HHH$. The spectrum of quasi real photons emitted by an energetic charged lepton beam can be described by the leading-order effective photon approximation (EPA)

$$\sigma_{EPA}(\ell^- A \to \ell^- X) = \int dx\; \mathcal{P}_{\gamma/\ell}(x)\; \hat{\sigma}(\gamma A), \tag{5}$$

where, for an energy fraction x of the charged lepton of initial energy E, the Weizsäcker-Williams spectrum is

* Mauro.Chiesa@unipv.it
† barbara.mele@roma1.infn.it
‡ fulvio.piccinini@pv.infn.it

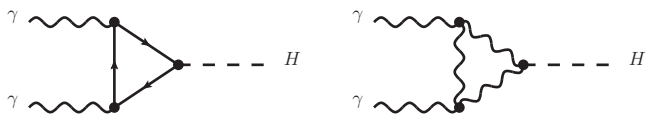

FIG. 1. Feynman diagrams contributing to the process $\gamma\gamma \to H$, involving top-quark and W-boson loops.

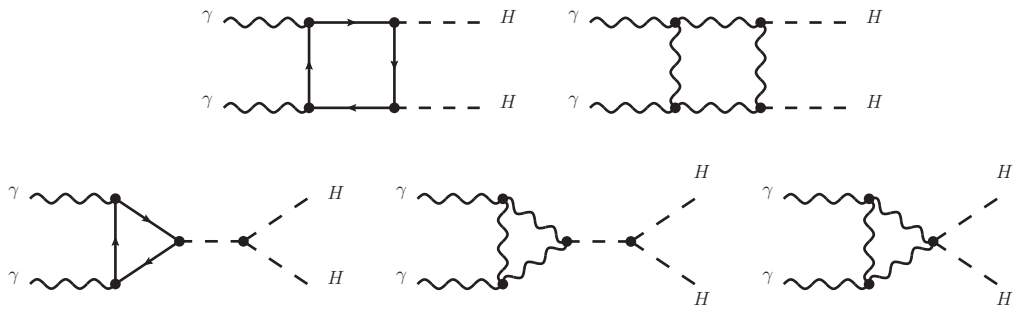

FIG. 2. Feynman diagrams contributing to the process $\gamma\gamma \to HH$, involving top-quark and W-boson loops.

given by [50, 51]

$$\mathcal{P}_{\gamma,\ell}(x) \approx \frac{\alpha}{2\pi} P_{\gamma,\ell}(x) \ln \frac{E^2}{m_\ell^2}, \tag{6}$$

with the splitting functions $P_{\gamma/\ell}(x) = (1 + (1-x)^2)/x$ for $\ell \to \gamma$, and $P_{\ell/\ell}(x) = (1+x^2)/(1-x)$ for $\ell \to \ell$.

We first analyze the total rates and kinematical features of the *partonic* processes $\gamma\gamma \to H, HH, HHH$. We then convolute them according to the EPA to obtain total rates and kinematical features of the corresponding processes $\mu^+\mu^- \to \mu^+\mu^-(H, HH, HHH)$, mediated by collinear photons. In EPA, the final muons will be forward and completely lost in the detector.

Our benchmark scenarios for muon collision c.m. energies $\sqrt{s}$ and corresponding integrated luminosities $\mathcal{L}$, according to a luminosity scaling $\mathcal{L} \sim 10\ \text{ab}^{-1}(\sqrt{s}/10\,\text{TeV})^2$ [1], will be

$$\sqrt{s} \simeq 3, 6, 10, 14, 30, 100\ \text{TeV}, \tag{7}$$

and

$$\mathcal{L} \sim 1, 4, 10, 20, 90, 1000\ \text{ab}^{-1}, \tag{8}$$

respectively [52].

In order to put the quite moderate photon-induced multi-Higgs production in context, we will compare the $\gamma\gamma$-induced $\mu^+\mu^- \to \mu^+\mu^-(H, HH, HHH)$ rates and distributions with the dominant ones for multi-Higgs production at tree-level [23, 24, 45, 47, 49]

$$\mu^+\mu^- \to \nu_\mu \bar{\nu}_\mu\,(H, HH, HHH), \tag{9}$$

$$\mu^+\mu^- \to \mu^+\mu^-(H, HH, HHH). \tag{10}$$

We stress that our numerical predictions for the processes in Eqs. (9)–(10) include complete tree-level matrix elements, i.e. the contribution of both vector-boson fusion (VBF) and s-channel production channels. However, since the VBF contribution is by far the dominant one at the c.m. energies in Eq. (7), we will dub the contributions in Eq. (9) and Eq. (10) as WW and ZZ fusion channels, respectively. The final neutrinos replacing muons in the WW-fusion channel will then mimic the photon induced process but with different kinematical features of the Higgs system. On the other hand, in the ZZ-fusion process, the final muons will be produced at an average $p_T^\mu \sim M_Z$, which will differentiate the ZZ-fusion signal from the $\gamma\gamma$-induced one. Indeed, we will show that in both the WW and ZZ fusion channels the transverse-momentum distribution for the H, HH, HHH systems has a maximum at p_T values of the order of the W, Z masses

$$p_T^{WW,ZZ}(H, HH, HHH) \sim M_{W,Z}, \tag{11}$$

which is typical of vector-boson fusion induced processes (see, e.g., [53], and [54] for single Higgs production in VBF). This will give a handle to separate the latter from the $\gamma\gamma$-induced signal that in the EPA in Eq. (6) is characterized by

$$p_T^{\gamma\gamma}(H, HH, HHH) \sim 0\,. \tag{12}$$

We will also compare the photon-induced loop production rates with other $\gamma\gamma$ multi-Higgs cross sections, where the Higgs bosons are radiated at tree-level by the intermediate amplitudes $\gamma\gamma \to W^{(*)}W^{(*)}$ and $\gamma\gamma \to t^{(*)}\bar{t}^{(*)}$, in the processes

$$\mu^+\mu^- \to \mu^+\mu^- W^+W^-(H, HH, HHH), \tag{13}$$

$$\mu^+\mu^- \to \mu^+\mu^- t\bar{t}\,(H, HH, HHH), \tag{14}$$

respectively, with forward (untagged) final muons. The two extra final W's and top quarks in Eqs. (13)–(14) will

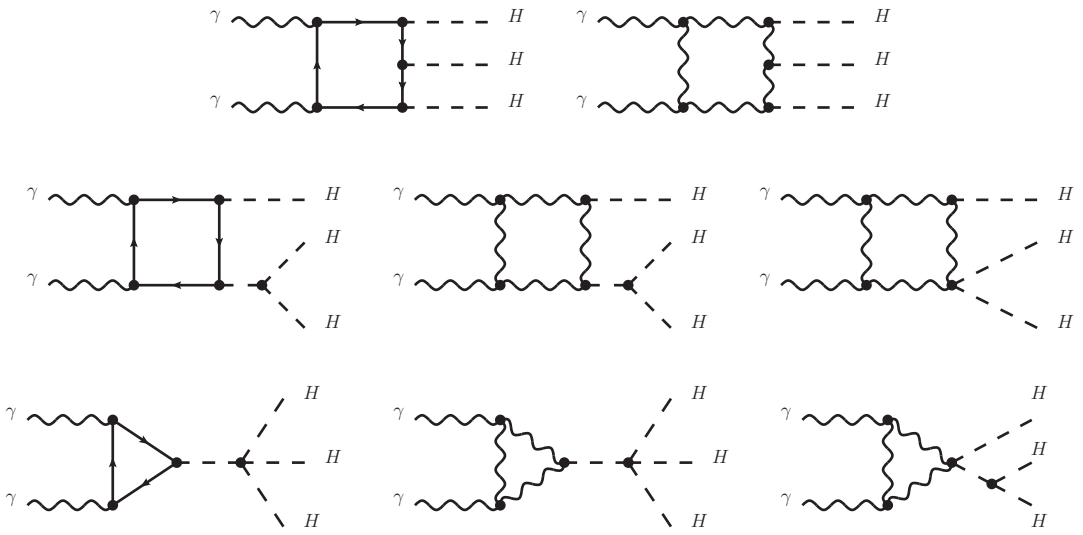

FIG. 3. Representative Feynman diagrams contributing to the process $\gamma\gamma \to HHH$, involving top-quark and W-boson loops.

of course distinguish these channels from the $\gamma\gamma$ loop production. We will see that, at particularly large $\sqrt{s}$ values, the production mechanism in Eq. (13) becomes dominant over the one-loop $\gamma\gamma$ fusion. On the other hand, the contributions in Eq. (14) are always smaller than the loop-induced ones in the setups under consideration.

The plan of the paper is the following. In Section 2, we describe the computational method used to obtain the photon-photon one-loop amplitudes and cross sections for multiple Higgs production. In Section 3, we study the partonic $\gamma\gamma \to (nH)$ cross sections and kinematical distributions versus $\sqrt{s}_{\gamma\gamma}$. The convoluted $\mu^+\mu^- \to \mu^+\mu^-\gamma^*\gamma^* \to \mu^+\mu^-(nH)$ cross sections (kinematical distributions) are considered in Section 4 (5), and compared with the corresponding VBF processes. In Section 6, we discuss a possible strategy to enhance the photon induced signal over the VBF production. We then study the sensitivity of the $\mu^+\mu^- \to \mu^+\mu^-\gamma^*\gamma^* \to \mu^+\mu^- HH$ cross section to a trilinear anomalous Higgs self-coupling, and of the $\mu^+\mu^- \to \mu^+\mu^-\gamma^*\gamma^* \to \mu^+\mu^- HHH$ cross section to a trilinear or quartic anomalous Higgs self-coupling in Section 7. Our conclusions are presented in Section 8.

II. CROSS SECTION COMPUTATIONAL METHOD

In this section we describe the procedure we followed to obtain the amplitudes and corresponding cross sections for the different processes described below.

The matrix elements for the loop-induced processes $\gamma\gamma \to H$, $\gamma\gamma \to HH$, and $\gamma\gamma \to HHH$ (cf. Figures 1-3) have been computed in a fully-automated way using the `Recola` library [55–58], which relies on the `Collier` library [59–62] for the evaluation of the tensor and scalar one-loop integrals.

For the phase-space integration, we used the Monte Carlo integrator already employed in [63, 64] for diboson production in hadronic collisions. In the Monte Carlo program, the proton PDFs have been replaced by a photon PDF describing the collinear $\mu \to \mu\gamma$ splitting as in Eq. (6), where m_ℓ is the muon mass and E is the nominal energy of the muon beam.

The same procedure has been followed to compute the cross sections for the tree-level processes $\gamma\gamma \to (nH)W^+W^-$ and $\gamma\gamma \to (nH)t\bar{t}$ ($n = 1, 2, 3$), relevant for the channels in Eqs. (13)–(14), and for the subsequent convolution with the photon PDF in the muon beams.

The tree-level results for $\mu^+\mu^- \to (H, HH, HHH)\nu_\mu\bar{\nu}_\mu$ via WW fusion, and $\mu^+\mu^- \to (H, HH, HHH)\mu^+\mu^-$ via ZZ fusion have been obtained by using the `Whizard` Monte Carlo event generator [65, 66]. In order to prevent singularities arising from s-channel diagrams, we include the gauge-boson widths in a gauge-invariant way by means of the complex-mass scheme [67–69]. We checked that, for these two classes of processes, the effect of s-channel diagrams is essentially dominated by the Z resonance region and it is numerically relevant only for the 3 TeV setup in Eq. (7), in particular for HHH production, while it becomes completely negligible when increasing the collider energy.

III. PARTONIC $\gamma\gamma$ CROSS SECTIONS

In this section, we discuss the total rates and kinematical distributions for the partonic channels $\gamma\gamma \to H, HH, HHH$, in the $\gamma\gamma$ c.m. system, before the convolution with the photon energy spectrum in the muon beams.

In the present approximation, the single Higgs channel

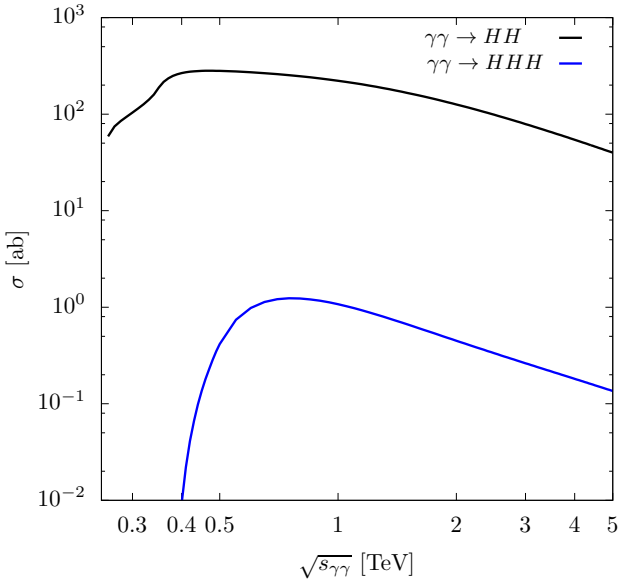

FIG. 4. Partonic total cross sections for the loop-induced processes $\gamma\gamma \to HH$ (black line), and $\gamma\gamma \to HHH$ (blue line) versus the $\gamma\gamma$ c.m. energy.

$\gamma\gamma \to H$ is characterized by a production rate resonating at the Higgs mass, $\sigma \sim \delta(\sqrt{s} - m_H)$, with the Higgs boson at rest in the $\gamma\gamma$ c.m. system. Once convoluted with the collinear photon spectrum in muon collisions, the final Higgs will still have zero transverse momentum, and a rapidity distribution that will just reflect the one of the initial $\gamma\gamma$ system.

As for the partonic $\gamma\gamma \to HH, HHH$ productions, we present in Figure 4 the corresponding total cross sections versus the $\gamma\gamma$ c.m. energy $\sqrt{s}_{\gamma\gamma}$, in the range $2m_H \lesssim \sqrt{s}_{\gamma\gamma} \lesssim 5$TeV. The two-Higgs cross section reaches its maximum value

$$\sigma_{max}(\gamma\gamma \to HH) \sim 0.28 \text{ fb} \quad \text{for} \quad \sqrt{s}_{\gamma\gamma} \sim 470 \text{ GeV}, \tag{15}$$

while the three-Higgs cross section has a maximum

$$\sigma_{max}(\gamma\gamma \to HHH) \sim 1.2 \text{ ab} \quad \text{for} \quad \sqrt{s}_{\gamma\gamma} \sim 750 \text{ GeV}. \tag{16}$$

The Higgs transverse-momentum, rapidity and angular distributions for the $\gamma\gamma \to HH$ process in the $\gamma\gamma$ c.m. system are shown in Figure 5, with the two Higgs bosons having the same energy $E_H = \sqrt{s}_{\gamma\gamma}/2$, and a back-to-back configuration.

Figure 6 shows the $\gamma\gamma \to HHH$ case (including the nontrivial Higgs energy distribution), by ordering the three final Higgs-bosons labels according to their transverse momentum.

IV. $\gamma\gamma$-INDUCED $\mu^+\mu^- \to \mu^+\mu^-(H, HH, HHH)$ CROSS SECTIONS

In this section, we present the $\mu^+\mu^-$ total cross sections for the $\gamma\gamma$-induced one-loop (H, HH, HHH) production after the convolution of the partonic cross section discussed in Section 3 with the photon spectrum described by the EPA in Eq. (6).

In Table I, the inclusive $\mu^+\mu^-$ cross sections (in ab) are presented versus $\sqrt{s}$, in the range 1.5 TeV $\lesssim \sqrt{s} \lesssim$ 100 TeV. For comparison, $\mu^+\mu^-$ cross sections for other *tree-level* (H, HH, HHH) production mechanisms mediated by tree-level $\gamma\gamma$ fusion ($\gamma\gamma \to (nH)W^+W^-$ and $\gamma\gamma \to (nH)t\bar{t}$, with $n = 1, 2, 3$), WW fusion ($WW \to H$, $WW \to HH$, and $WW \to HHH$), and ZZ fusion ($ZZ \to H$, $ZZ \to HH$, and $ZZ \to HHH$) are also detailed.

Regarding the single Higgs boson production, one can see that the $\gamma\gamma \to H$ cross section varies in the range $\sigma_{(\gamma\gamma\to H)} \sim [0.2 - 1.6]$ fb. At $\sqrt{s} \sim 14$ TeV, $\sigma_{(\gamma\gamma\to H)} \sim$ 0.78 fb, which, with the benchmark integrated luminosity of 20 ab^{-1} in Eq. (8), would correspond to about 16.000 events. At $\sqrt{s} \sim 3$ TeV with 1 ab^{-1}, one has $\sigma_{(\gamma\gamma\to H)} \sim 0.37$ fb, corresponding to about 400 events. These rates are about 3 and 2 orders of magnitude less than, respectively, the $WW \to H$ and $ZZ \to H$ ones for all $\sqrt{s}$ values.

As for double Higgs boson production, the $\gamma\gamma \to HH$ cross section varies in the range $\sigma_{(\gamma\gamma\to HH)} \sim [0.4 - 8]$ ab. At $\sqrt{s} \sim 14$ TeV, $\sigma_{(\gamma\gamma\to HH)} \sim 3$ ab, which, with 20 ab^{-1}, would correspond to about 60 events. At $\sqrt{s} \sim 3$ TeV with 1 ab^{-1}, one has $\sigma_{(\gamma\gamma\to HH)} \sim 0.9$ ab, corresponding to about 1 event. Similarly to single Higgs production, these HH rates are, about 3 and 2 orders of magnitude less than, respectively, the $WW \to HH$ and $ZZ \to HH$ ones for all $\sqrt{s}$ values.

Finally, for triple Higgs boson production, the $\gamma\gamma \to HHH$ cross section varies in the range $\sigma_{(\gamma\gamma\to HHH)} \sim [0.07 - 2.3] \times 10^{-2}$ ab, and requires the maximum c.m. energy to become observables. Indeed, at $\sqrt{s} \sim 14$ TeV, $\sigma_{(\gamma\gamma\to HHH)} \sim 8.4 \times 10^{-3}$ ab, which, with 20 ab^{-1}, would correspond to no event produced, just as in the case of $\sqrt{s} \sim 3$ TeV (with 1 ab^{-1}), where one has $\sigma_{(\gamma\gamma\to HHH)} \sim 2 \times 10^{-3}$ ab. On the other hand, at $\sqrt{s} \sim 30$ TeV, $\sigma_{(\gamma\gamma\to HHH)} \sim 1.3 \times 10^{-2}$ ab, which, with 90 ab^{-1}, would correspond to about one event. Hence, only going to the very upper $\sqrt{s}$ range considered here, one could have an observable event number. I particular, at $\sqrt{s} \sim 100$ TeV with 10^3 ab^{-1}, $\sigma_{(\gamma\gamma\to HHH)} \sim 2.3 \times 10^{-2}$ ab, one would give about 23 events. Note that, at low $\sqrt{s}$ values, the HHH rates are less depleted than in the case of H and HH production with respect to VBF production, being only about 2 and 1 orders of magnitude less than the $WW \to HHH$ and $ZZ \to HHH$ ones, respectively.

The behavior of $\mu^+\mu^-$ total rates versus $\sqrt{s}$ is more clearly shown in Figure 7, where for comparison also VBF cross sections are plotted. In the left plot the

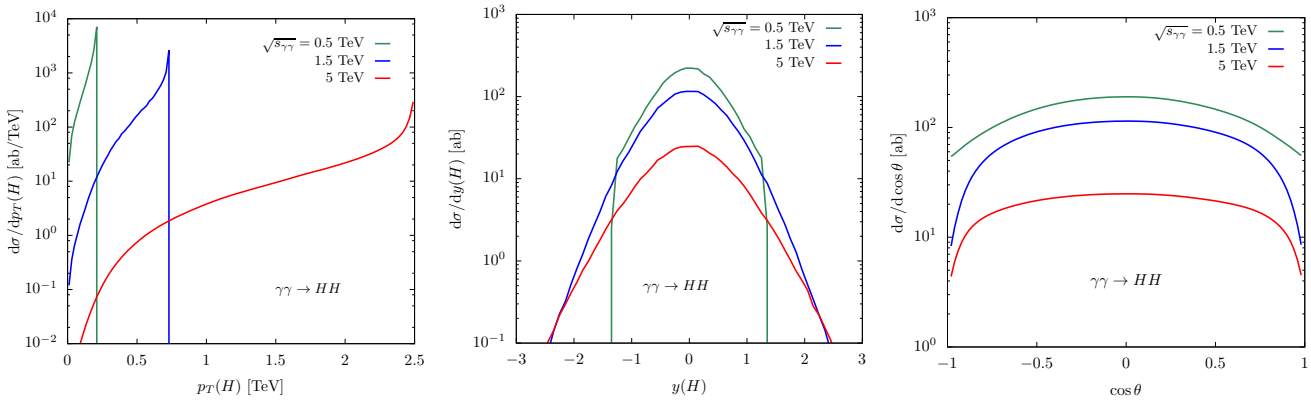

FIG. 5. Higgs transverse-momentum (left), rapidity (center), and angular (right) distributions for the loop-induced process $\gamma\gamma \to HH$ in photon collisions, in the $\gamma\gamma$ c.m. system, for three values of the $\gamma\gamma$ c.m. energy.

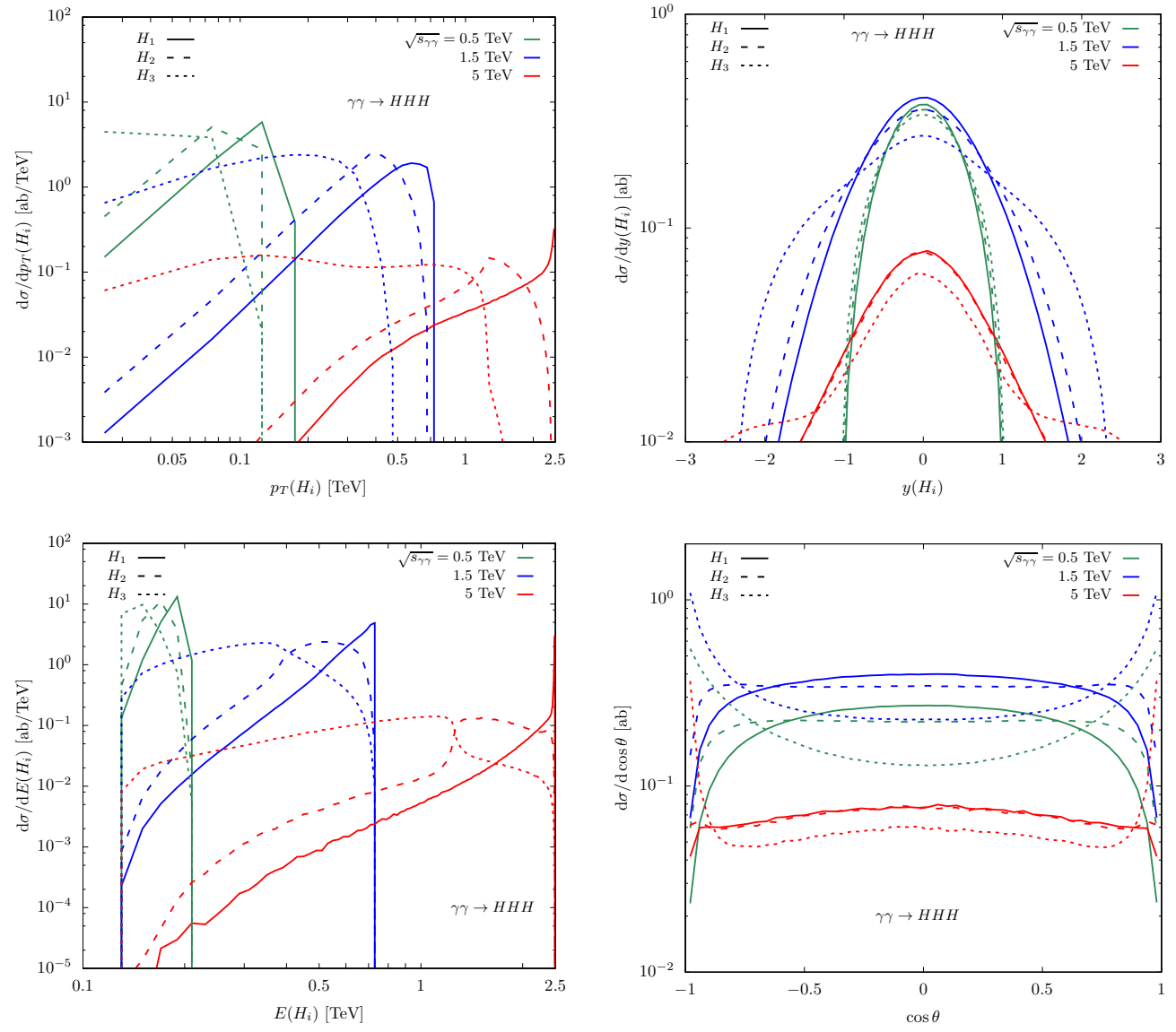

FIG. 6. Higgs transverse-momentum (upper left), rapidity (upper right), energy (lower left), and angular (lower right) distributions for the loop-induced process $\gamma\gamma \to HHH$ in photon collisions, in the $\gamma\gamma$ c.m. system, for three values of the $\gamma\gamma$ c.m. energy. The H_i label ($i = 1, 2, 3$) refers to the Higgs bosons ordered in p_T, with H_1 labelling the highest-p_T Higgs.

$\mu^+\mu^- \to H\mu^+\mu^-$ production (blue solid line) is compared with the same process when replacing $\mu^\pm \to e^\pm$ (blue dashed line), and with WW-fusion (red solid line), ZZ-fusion (green solid line) single-Higgs production, for $\sqrt{s} \lesssim 400$ GeV. The difference of about a factor three in the rates for the electron and muon initiated processes for $\gamma\gamma$ fusion stems from the double logarithm arising from Eq. 6 applied twice to initial beams. The dashed red and green lines represent the integrated cross-sections for single Higgs productions in *pure* WW and ZZ fusion, respectively, in μ^+e^- scattering: in practice, since both electrons and muons in our simulations are treated as massless particles (with the only exception of the mass parameter in the photon spectrum in Eq. (6)), these lines correspond to the predictions for H production in WW and ZZ fusion when only the t-channel production mechanism is considered. The difference between red (green) solid and dashed lines is large at the opening of the Z resonance ($\sqrt{s} \sim M_H + M_Z$) and decreases for larger values of $\sqrt{s}$.

In the right plot of Figure 7, $\mu^+\mu^-$ collision rates for the H (solid lines), HH (dashed lines), HHH (dot-dashed lines) one-loop $\gamma\gamma$ production (blue lines) are shown, and compared with the corresponding rates for tree-level WW-fusion (red lines), and ZZ fusion (green lines) production, for 1 TeV $\lesssim \sqrt{s} \lesssim$ 100 TeV.

V. HIGGS BOSON DISTRIBUTIONS IN $\gamma\gamma$-INDUCED HH AND HHH PRODUCTION

In this section, we go through the main kinematical features of the Higgs bosons in $\gamma\gamma$-induced $\mu^+\mu^- \to \mu^+\mu^-(HH, HHH)$ production. We first present the inclusive Higgs kinematical distributions. Then we include the effect of a reduced acceptance in the Higgs kinematics due to a possible shielding of the detector in the forward regions, where the *beam-induced background* (BIB) might become prohibitive [70–77]. To this end, we will assume a two-body decay of the produced Higgs (giving the dominant contribution to the Higgs decay width, through the channels $H \to b\bar{b}, c\bar{c}, gg, \tau\tau$), and put a minimum transverse-momentum cut and a maximum rapidity cut on the Higgs decay products (applying no decay branching ratio). In particular, we simulate the effect of introducing "shielding nozzles" in the detector, by assuming a detector coverage for all kind of particles only for transverse momentum and rapidity $p_T > 20$ GeV, $|y| < 3$.

As for the single Higgs production, in the present approximation, the Higgs kinematics simply reflects the rapidity distribution of the initial $\gamma\gamma$ system as provided by the collinear photon spectrum described by the EPA in Eq. (6), which gives vanishing Higgs transverse momentum.

The inclusive Higgs transverse-momentum and rapidity distributions for the two Higgs production in $\mu^+\mu^- \to \mu^+\mu^- HH$ mediated by $\gamma^*\gamma^* \to HH$ are presented in Figure 8, for different values of $\sqrt{s}$. The same distributions for the three Higgs production in $\mu^+\mu^- \to \mu^+\mu^- HHH$ mediated by $\gamma^*\gamma^* \to HHH$ are shown in Figure 9, where H_1 labels the highest-p_T Higgs, and H_2 the second highest-p_T Higgs.

In Figure 10, we present instead the photon-induced $\mu^+\mu^- \to \mu^+\mu^- HH$ Higgs transverse-momentum and rapidity distributions after applying the selection cuts $p_T^b > 20$ GeV, $|y_b| < 3$ on the $H \to b\bar{b}$ decay products (blue lines), at $\sqrt{s} = 3, 10, 30$ TeV. For comparison, the same distributions for the tree-level WW channel (red lines) and ZZ channel (green lines) are also shown. For the process $\mu^+\mu^- \to \mu^+\mu^- HH$, calculated with EPA, both Higgs bosons have the same transverse momentum and therefore only the blue solid line is shown.

Similarly, in Figure 11, we present the $\mu^+\mu^- \to \gamma^*\gamma^*\mu^+\mu^- \to \mu^+\mu^- HHH$ case. As anticipated, no Higgs decay BR is applied in Figure 10 and 11.

VI. ENHANCING THE $\gamma\gamma \to n\,H$ SIGNAL OVER THE $WW, ZZ \to n\,H$ BACKGROUND

The previous discussion clearly shows that one-loop $\gamma\gamma \to H, HH, HHH$ production in $\mu^+\mu^-$ collisions is quite suppressed with respect to the $WW, ZZ \to H, HH, HHH$ production. Independently of that, a $\gamma\gamma \to HHH$ signal can be considered statistically out of reach even for the most optimistic luminosities scenarios. On the other hand, the higher statistics channels $\gamma\gamma \to H, HH$, being suppressed by orders of magnitudes with respect to $WW, ZZ \to H, HH$ production, will be in general overwhelmed by the latter, making the detection of loop-induced events quite hard in general. In this section we propose a strategy that could dramatically enhance a $\gamma\gamma \to H, HH, HHH$ signal over the VBF ones.

It is well know that VBF single Higgs production is characterized by a typical Higgs transverse momentum of the order of the $M_{W,Z}$ [Eq. (11)]. This feature is shared by VBF *multiple* Higgs production, and is connected to the mechanism of vector-boson radiation from the initial beams.

In Figure 12, we show the transverse-momentum distribution of the HH (solid lines) and HHH (dashed lines) systems in VBF-mediated HH and HHH production, respectively, in $\mu^+\mu^-$ collisions, at various $\sqrt{s}$. The transverse-momentum distribution for the HH and HHH systems indeed keeps the single Higgs VBF production main feature, with a maximum at $p_T(HH, HHH) \sim M_{W,Z}$. This should be confronted with the $\gamma\gamma$ one-loop process where, in the approximation of Eq. (6), one has $p_T(H, HH, HHH) \sim 0$.

In order to enhance the $\gamma\gamma$ signal over the VBF one, one can then impose, depending on the momentum resolution $\Delta p_T(n\,H)$ of the detector, a cut on large $p_T(n\,H)$ events (that is events characterized by $p_T(n\,H) \gtrsim \Delta p_T(n\,H)$), which leaves unsuppressed the photon-induced $p_T(n\,H) \sim 0$ events. In this way, the

$\sqrt{s}$ [TeV]	1.5	3	6	10	14	30	100
$\sigma(\mu^+\mu^-)$ [ab]							
$\gamma\gamma \to H$	2.35×10^{2}	3.66×10^{2}	5.29×10^{2}	6.71×10^{2}	7.76×10^{2}	1.05×10^{3}	1.58×10^{3}
$\gamma\gamma \to HWW$	5.40×10^{1}	2.88×10^{2}	9.93×10^{2}	2.08×10^{3}	3.20×10^{3}	7.46×10^{3}	2.20×10^{4}
$\gamma\gamma \to Ht\bar{t}$	9.53×10^{-1}	3.27	7.53	1.21×10^{1}	1.57×10^{1}	2.61×10^{1}	4.82×10^{1}
$\mu^+\mu^- \to H\nu\bar{\nu}$	3.11×10^{5}	4.98×10^{5}	6.96×10^{5}	8.44×10^{5}	9.43×10^{5}	1.17×10^{6}	1.52×10^{6}
$\mu^+\mu^- \to H\mu^+\mu^-$	3.13×10^{4}	5.08×10^{4}	7.16×10^{4}	8.73×10^{4}	9.78×10^{4}	1.21×10^{5}	1.59×10^{5}
$\gamma\gamma \to HH$	3.77×10^{-1}	9.00×10^{-1}	1.70	2.47	3.07	4.67	7.96
$\gamma\gamma \to HHWW$	5.63×10^{-3}	8.16×10^{-2}	5.72×10^{-1}	1.79	3.43	1.21×10^{1}	5.86×10^{1}
$\gamma\gamma \to HHt\bar{t}$	1.72×10^{-3}	9.15×10^{-3}	2.57×10^{-2}	4.55×10^{-2}	6.25×10^{-2}	1.14×10^{-1}	2.33×10^{-1}
$\mu^+\mu^- \to HH\nu\bar{\nu}$	2.43×10^{2}	8.48×10^{2}	2.05×10^{3}	3.38×10^{3}	4.47×10^{3}	7.60×10^{3}	1.44×10^{4}
$\mu^+\mu^- \to HH\mu^+\mu^-$	3.22×10^{1}	1.12×10^{2}	2.72×10^{2}	4.50×10^{2}	5.96×10^{2}	1.02×10^{3}	1.94×10^{3}
$\gamma\gamma \to HHH$	7.13×10^{-4}	2.11×10^{-3}	4.38×10^{-3}	6.63×10^{-3}	8.38×10^{-3}	1.31×10^{-2}	2.30×10^{-2}
$\gamma\gamma \to HHHWW$	2.57×10^{-6}	3.69×10^{-5}	2.69×10^{-4}	9.76×10^{-4}	2.15×10^{-3}	1.07×10^{-2}	$8.5(1)\times10^{-2}$
$\gamma\gamma \to HHHt\bar{t}$	3.79×10^{-6}	4.03×10^{-5}	1.39×10^{-4}	2.67×10^{-4}	3.83×10^{-4}	7.50×10^{-4}	1.66×10^{-3}
$\mu^+\mu^- \to HHH\nu\bar{\nu}$	9.90×10^{-2}	3.44×10^{-1}	1.66	4.19	7.02	1.85×10^{1}	5.82×10^{1}
$\mu^+\mu^- \to HHH\mu^+\mu^-$	1.66×10^{-2}	5.91×10^{-2}	2.91×10^{-1}	7.37×10^{-1}	1.24	3.26	1.03×10^{1}

TABLE I. Inclusive $\mu^+\mu^-$ cross sections (in ab) for photon-induced one-loop $\gamma\gamma \to H, HH, HHH$ production versus $\mu^+\mu^-$ c.m. energy. For comparison, $\mu^+\mu^-$ cross sections for other (H, HH, HHH) tree-level production mechanisms mediated by $\gamma\gamma$ $[\gamma\gamma \to (nH)W^+W^-$ and $\gamma\gamma \to (nH)t\bar{t}]$ and the ones for the processes $\mu^+\mu^- \to (nH)\nu\bar{\nu}$ and $\mu^+\mu^- \to (nH)\mu^+\mu^-$ $(n = 1, 2, 3)$ are also detailed.

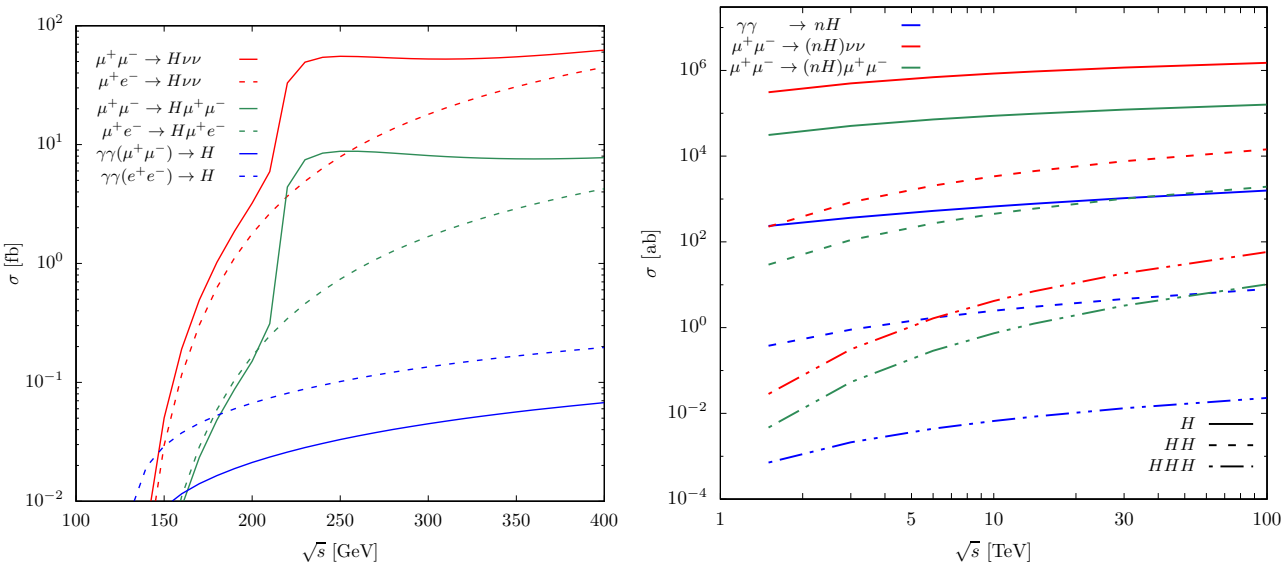

FIG. 7. Inclusive $\mu^+\mu^-$ cross sections for one-loop $\gamma\gamma \to H, HH, HHH$ production versus $\mu^+\mu^-$ c.m. energy. In the left plot the photon-induced single Higgs $\mu^+\mu^- \to H\mu^+\mu^-$ production (blue solid line) is compared with the same process for $\mu^\pm \to e^\pm$ (blue dashed line), and with the tree-level processes $\mu^+\mu^- \to H\nu\bar{\nu}$ (red solid line) and $\mu^+\mu^- \to H\mu^+\mu^-$ (green solid line) , for $\sqrt{s} \lesssim 400$ GeV. The dashed red and green lines represent the integrated cross-sections for single Higgs productions in WW and ZZ fusion, respectively, in μ^+e^- scattering. In the right plot, $\mu^+\mu^-$ cross sections for the H (solid lines), HH (dashed lines), HHH (dot-dashed lines) $\gamma\gamma$-mediated one-loop production (blue lines) are compared with the corresponding total rates for WW-fusion (red lines), and ZZ fusion (green lines) production, for 1 TeV $\lesssim \sqrt{s} \lesssim 100$ TeV.

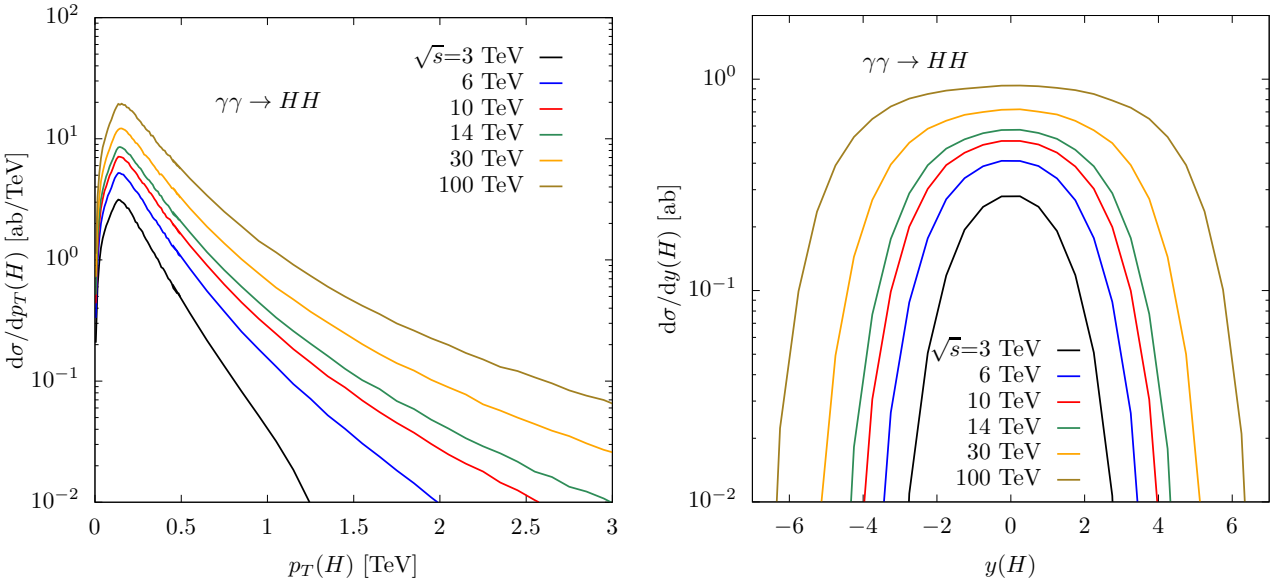

FIG. 8. Higgs transverse-momentum (left plot) and rapidity (right plot) distributions for the two-Higgs photon-induced production in $\mu^+\mu^- \to \mu^+\mu^- HH$, versus $\sqrt{s}$.

actual background from VBF events is reduced to the sub-dominant fraction of events characterized by a small $p_T(n\,H)$, hopefully as small as much less than $\mathcal{O}(M_W)$.

Figure 13 shows the effects on $\mu^+\mu^-$ total rates of a cut-flow selecting low $n\,H$ transverse-momentum events. The $n\,H$ transverse-momenta are reconstructed by summing up the vectorial momenta of the $H \to b\bar{b}$ decay products, assuming the finite acceptance $p_T^b > 20$ GeV, $|y_b| < 3$ (not including any decay BR) . Then, the inclusive cross sections for the $n\,H$ processes (solid lines) are compared with the production rates that pass the $H \to b\bar{b}$ basic acceptance cuts (dashed lines), and with the rates where a further constrain on the maximum $n\,H$ transverse-momentum (as reconstructed from the Higgs decay products) is applied (dot-dashed lines). Two cases are analyzed for the maximum $n\,H$ transverse-momentum, which are $p_T(n\,H) \lesssim 10$ GeV (left plot), and 30 GeV (right plot).

Figure 13 clearly shows how a cut on large transverse momentum of the Higgs system can upset the hierarchy of the rates for the $\gamma\gamma$ and VBF processes, hence allowing to control the VBF background to multiple Higgs $\gamma\gamma$ production. In particular, in the $p_T(n\,H) \lesssim 10$ GeV case (left plots), one can see that after the acceptance cuts the $\gamma\gamma$ single Higgs production gets comparable to the ZZ channel at all $\sqrt{s}$, while both the double and triple Higgs $\gamma\gamma$ productions get the upper-hand over the ZZ channels. The WW channel is maintained moderately dominant over $\gamma\gamma$ for both H and HH productions, and gets comparable to $\gamma\gamma$ in HHH production. The VBF background suppression gets of course less dramatic by relaxing the $p_T(n\,H)$ to 30 GeV (Figure 13, right plots).

VII. CROSS SECTION SENSITIVITIES TO ANOMALOUS HIGGS SELF-COUPLINGS

Before concluding, we want to briefly discuss the sensitivity of the $\gamma\gamma \to HH, HHH$ cross sections to possible anomalies in the Higgs boson self-interactions. In particular, we will assume a deviation in either the trilinear Higgs coupling $\lambda_3(1+\delta_3)HHH$ or the quartic Higgs coupling $\lambda_4(1+\delta_4)HHHH$, where $\lambda_{3,4}$ are the self-coupling SM values, and $\delta_{3,4} \neq 0$ would reveal possible deviations BSM in the Higgs potential. We leave a more sophisticated analysis performed in terms of effective-field theories for future work. In Figure 14, left plot, we detail the ratio of the $\gamma\gamma \to HH$ total cross section with and without anomalous Higgs self-couplings versus δ_3 at different muon collision $\sqrt{s}$, while, in the right plot, we show the same quantity after applying the acceptance cuts on Higgs decays. At the level of inclusive quantities, there is a good sensitivity to anomalous trilinear coupling of the double Higgs production. In particular, a $\delta_3 \simeq \pm 1$ variation increases the cross sections by about 15–20%. After imposing the acceptance cuts, the sensitivity is in general slightly reduced

In Figure 15 we show the δ_3 dependence for $\delta_4 = 0$ (upper plots), and δ_4 dependence for $\delta_3 = 0$ (lower plots) for the ratio of the cross sections for triple Higgs production with and without anomalous couplings via photon scattering at different muon $\sqrt{s}$. The results corresponding to the setups with (right plots) and without (left plots) acceptance cuts are shown. Note that for the reference integrated luminosities in Eq. (8), the tiny $\gamma\gamma \to HHH$ production cross section will not allow a precision cross-section measurement. However, as in the case of double Higgs production, there is a sizeable dependence on

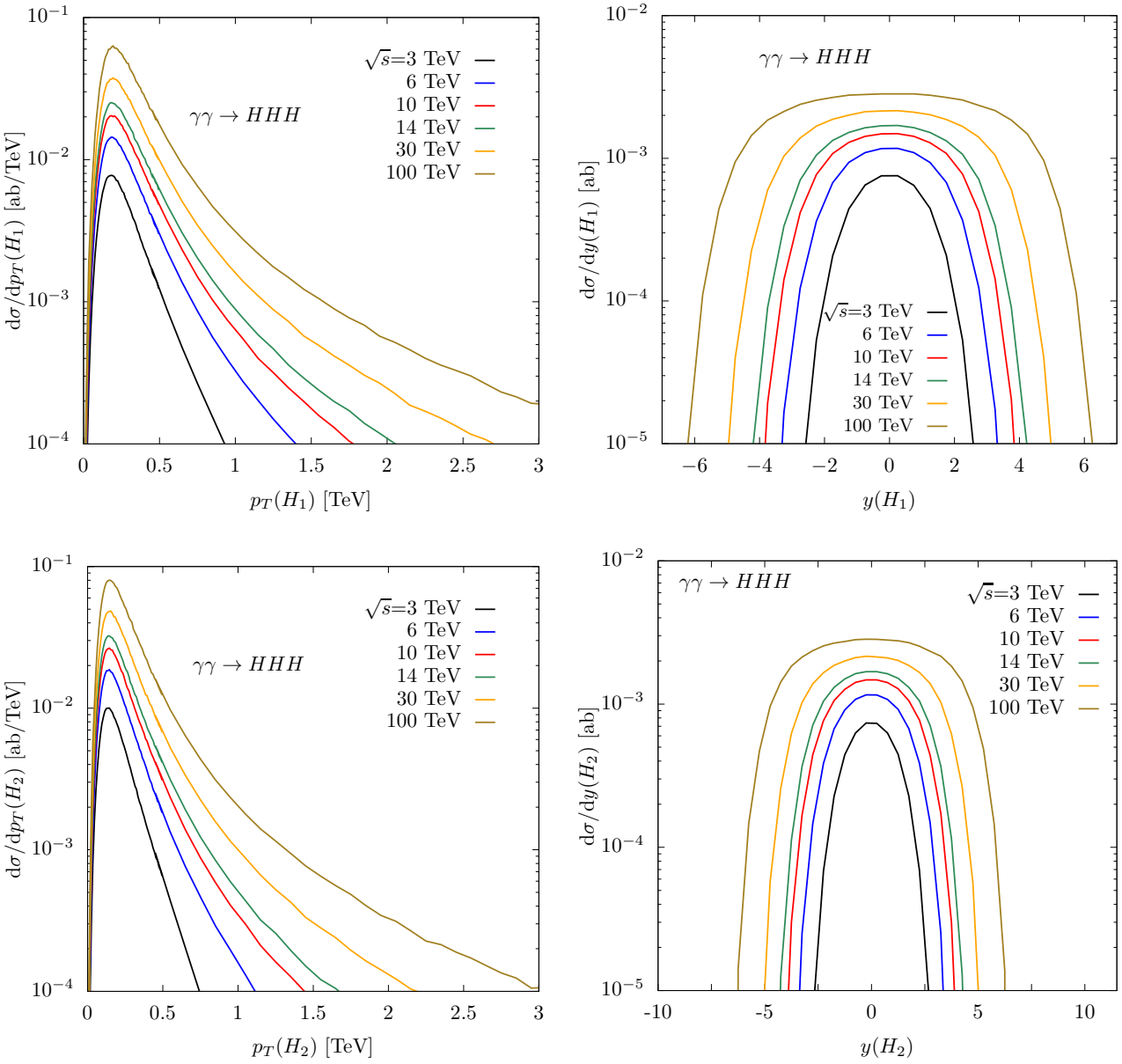

FIG. 9. Higgs transverse-momentum (left plots) and rapidity (right plots) distributions for the three-Higgs photon-induced production in $\mu^+\mu^- \to \mu^+\mu^- HHH$, versus $\sqrt{s}$. $H_{1(2)}$ labels the (second) highest-p_T Higgs.

anomalous Higgs self-couplings, in particular for coupling variations of the order of $\delta_{3(4)} \sim \pm 1$, at $\delta_{4(3)} \simeq 0$. Furthermore, $\gamma\gamma \to HHH$ cross section has a minimum around its SM value for $\delta_4 \sim 0$ and variable δ_3, while the δ_4 dependence is monotonic in the δ_4 range considered in Figure 15 (lower plots). We checked that the latter monotonic δ_4 dependence is the outcome of a nontrivial interplay between the top-loop and the W-loop amplitudes providing the final sensitivity to anomalous δ_4.

VIII. CONCLUSIONS

Single, double and triple Higgs-boson production mediated by photon fusion via loops of heavy particles (top quarks and W bosons) have been studied at multi-TeV lepton colliders. For integrated collision luminosities scaling as $\mathcal{L} \sim 10\,\text{ab}^{-1}(\sqrt{s}/10\,\text{TeV})^2$, at $\sqrt{s} \sim 14(3)$ TeV one has inclusive cross sections corresponding to 16.000 (400) single Higgs events and 60 (1) double Higgs events, while triple Higgs production is quite suppressed, and needs $\sqrt{s} \gtrsim 30$ TeV for getting more than 1 HHH event. We have studied kinematical distributions at different $\sqrt{s}$, and analyzed the effects of a finite acceptance on the Higgs decay products in order to control BIB effects

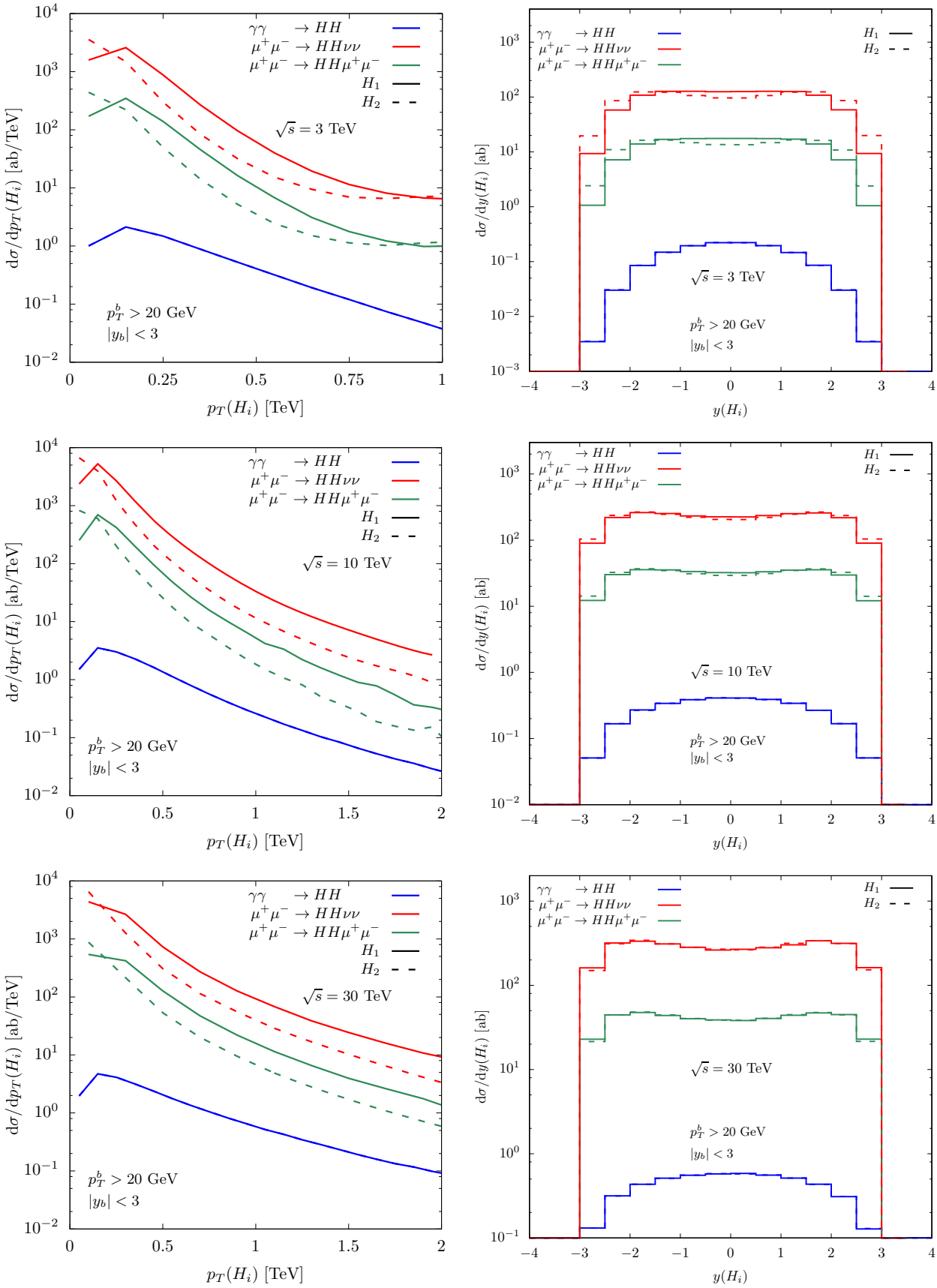

FIG. 10. Higgs transverse-momentum (left plots) and rapidity (right plots) distributions for the two-Higgs photon-induced production in $\mu^+\mu^- \to \mu^+\mu^- HH$, at different $\sqrt{s}$, after imposing a limited geometric acceptance for the Higgs two-body decay products. $H_{1(2)}$ labels the (second) highest-p_T Higgs. The same distributions for the $\mu^+\mu^- \to HH\nu\bar{\nu}$ and $\mu^+\mu^- \to HH\mu^+\mu^-$ tree-level channels are shown for comparison.

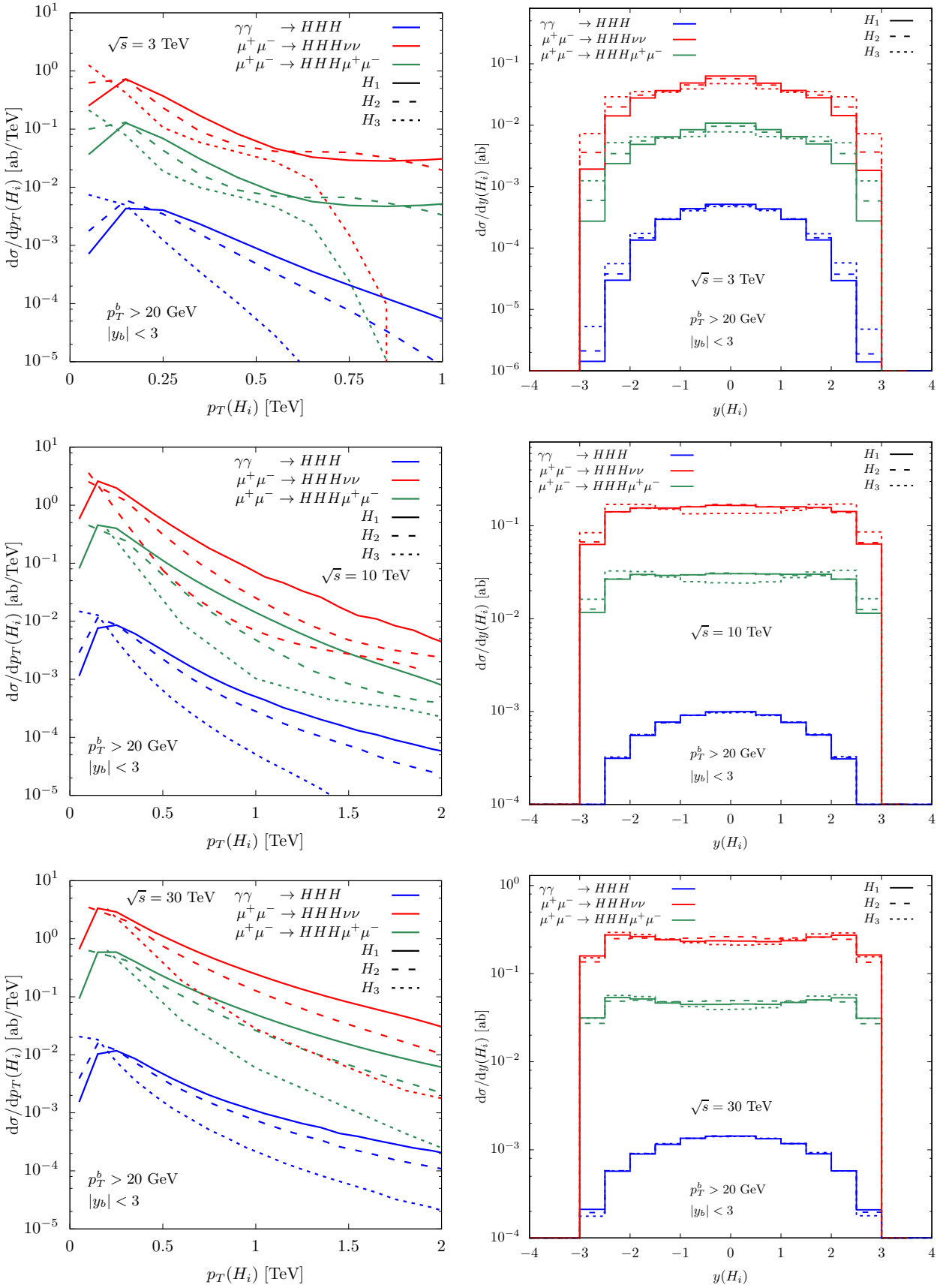

FIG. 11. Higgs transverse-momentum (left plots) and rapidity (right plots) distributions for the triple-Higgs photon-induced production in $\mu^+\mu^- \to \mu^+\mu^- HHH$, at different $\sqrt{s}$, after imposing a limited geometric acceptance for the Higgs two-body decay products. $H_{1(2/3)}$ labels the (second/third) highest-p_T Higgs. The same distributions for the $\mu^+\mu^- \to HHH\nu\bar{\nu}$ and $\mu^+\mu^- \to HHH\mu^+\mu^-$ tree-level channels are shown for comparison.

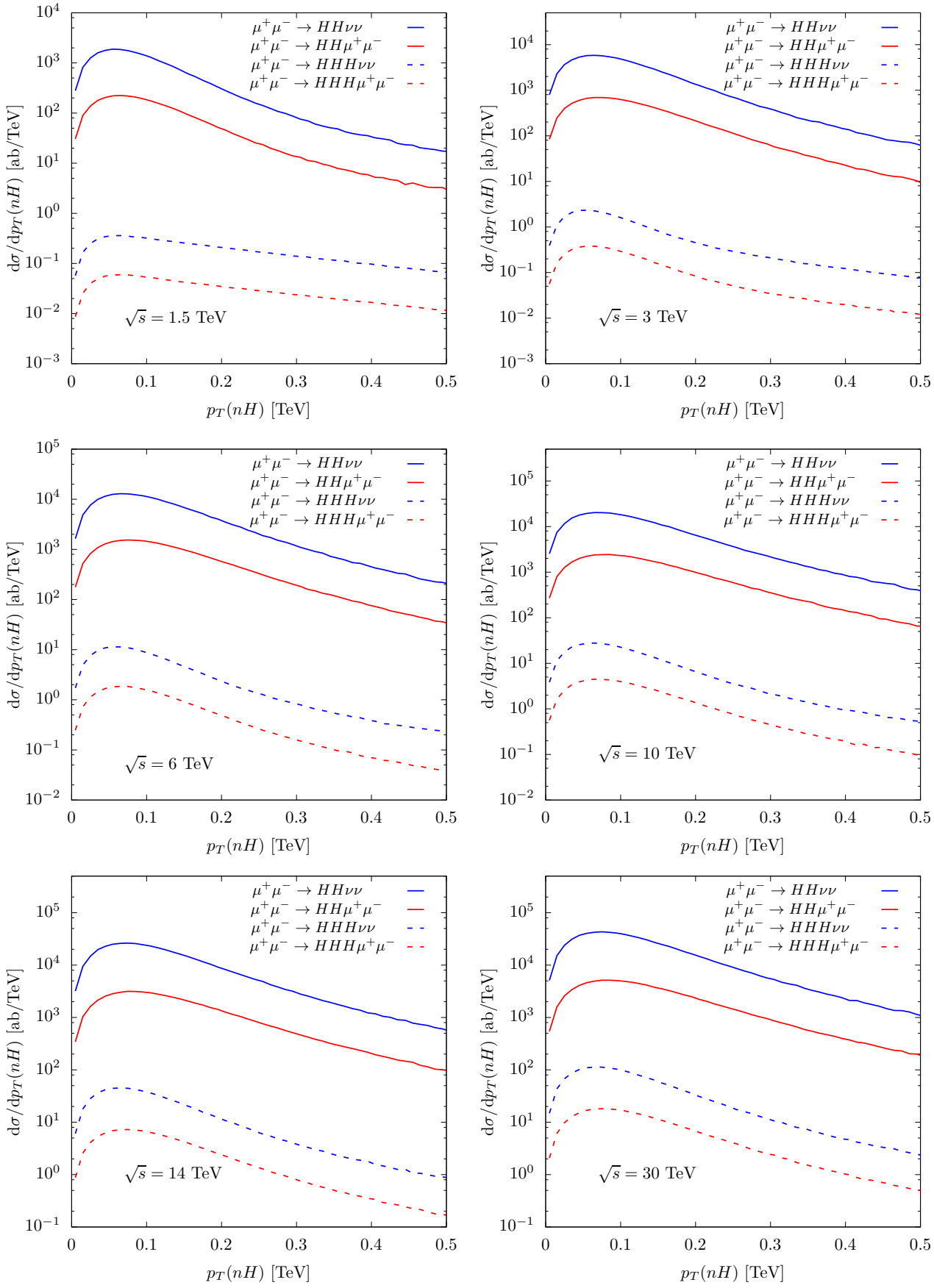

FIG. 12. Transverse-momentum distribution of the HH (solid lines) and HHH (dashed lines) systems in vector-boson-fusion mediated double and triple Higgs production, respectively, in muon collisions, at different $\sqrt{s}$.

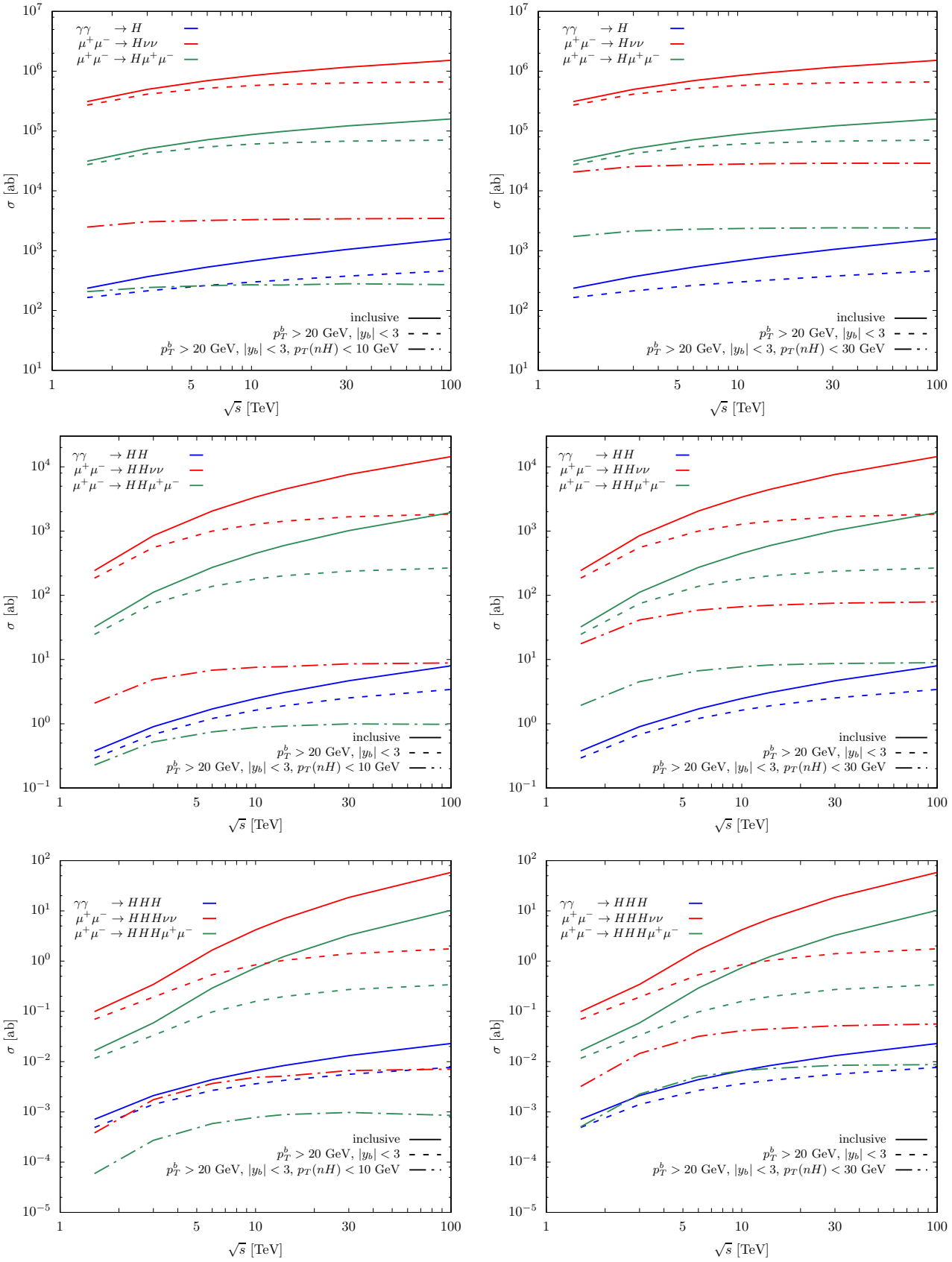

FIG. 13. Effects of the cut-flow selecting low $n\,H$ transverse-momentum events. The $\mu^+\mu^-$ inclusive cross section for the $n\,H$ processes (solid lines) are compared with the production rates that pass the Higgs decays basic acceptance (dashed lines), and with the rates where a further constrain on the maximum $n\,H$ transverse-momentum (as reconstructed from Higgs decay products) is applied (dot-dashed lines), which is 10 GeV in the left plot, and 30 GeV in the right plot.

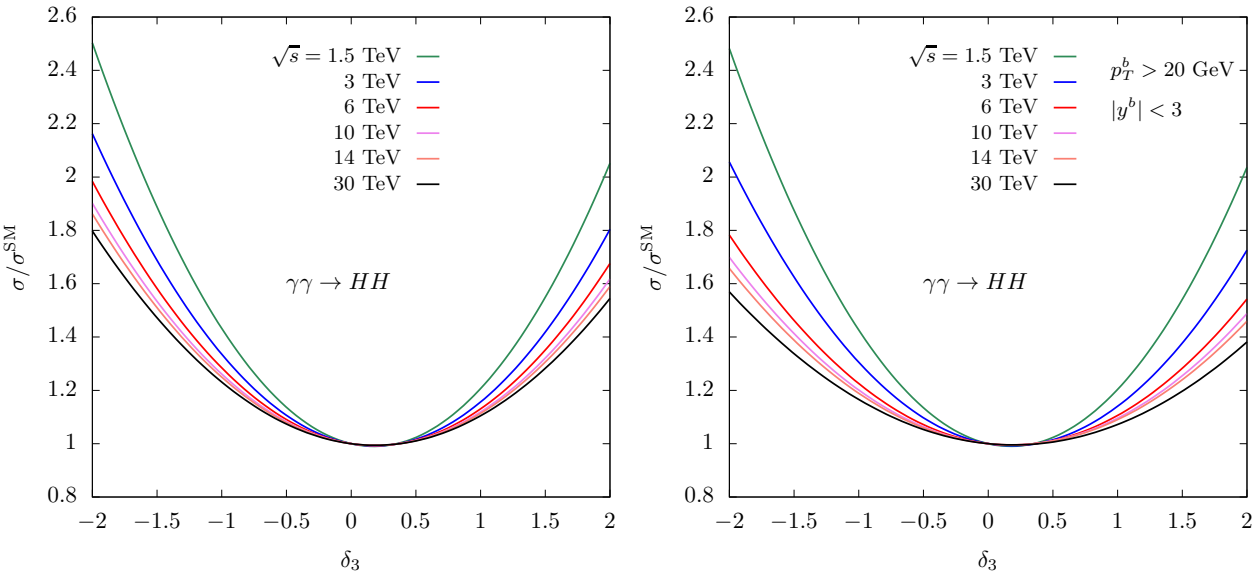

FIG. 14. Ratio of the integrated cross sections with and without anomalous Higgs self-couplings for the process $\gamma\gamma \to HH$ in the inclusive setup (left plot) and after imposing acceptance cuts on the Higgs decay products (right plot) as a function of δ_3.

via dead cones along the beams. The comparison with the dominant VBF mechanism for producing single, double and triple Higgs final states has been carried out, and possible strategies for pinpointing $\gamma\gamma$-induced events on the basis of the total transverse momentum of the Higgs system have been suggested. Finally, the inclusive cross sections sensitivity to triple and quartic Higgs self-couplings have been discussed and found sizeable.

Multi-TeV muon colliders offer a unique possibility to probe such processes. Apart from single Higgs production, which has been discussed at future e^+e^- colliders [78], we are not aware of any similar study at multi-TeV future colliders [79] allowing to compare the corresponding potential for multi-Higgs production induced by quasi-real photon collisions.

Our study proceeded under the strict assumption of collinear initial photons described by means of the EPA, which is valid in first approximation. A more refined analysis should relax this assumption, and consider in $\gamma\gamma$ one-loop multi-Higgs production also interference and coherence effects with Z-boson mediated processes described in terms of electroweak PDFs [53]. This would imply including at the amplitude level both VBF ZZ fusion channels (possibly including higher-order EW corrections) and one-loop γZ-induced channels. However, the effects of the latter two processes should affect mainly non-vanishing $p_T(nH)$ final states, and the description in terms of collinear EW PDFs might need to be improved to better describe the transverse momenta of the initial-state vector bosons. We then leave an extensive discussion of this issue to further dedicated studies.

ACKNOWLEDGMENTS

We thank Fabio Maltoni for useful discussions.

[1] J. P. Delahaye, M. Diemoz, K. Long, B. Mansoulié, N. Pastrone, L. Rivkin, D. Schulte, A. Skrinsky, and A. Wulzer, "Muon Colliders," arXiv:1901.06150 [physics.acc-ph].
[2] V. Shiltsev and F. Zimmermann, Rev. Mod. Phys. **93**, 15006 (2021), arXiv:2003.09084 [physics.acc-ph].
[3] V. Shiltsev, in *2nd North American Particle Accelerator Conference* (2017) arXiv:1705.02011 [physics.acc-ph].
[4] G. I. Budker, Conf. Proc. C **690827**, 33 (1969).
[5] C. M. Ankenbrandt *et al.*, Phys. Rev. ST Accel. Beams **2**, 081001 (1999), arXiv:physics/9901022.
[6] R. B. Palmer, Rev. Accel. Sci. Tech. **7**, 137 (2014).
[7] M.-H. Wang, Y. Nosochkov, Y. Cai, and M. Palmer, JINST **11**, P09003 (2016).
[8] Y. Alexahin, E. Gianfelice-Wendt, and V. Kapin, JINST **13**, P11002 (2018), arXiv:1806.08717 [physics.acc-ph].
[9] M. Boscolo, J.-P. Delahaye, and M. Palmer, Rev. Accel. Sci. Tech. **10**, 189 (2019), arXiv:1808.01858 [physics.acc-ph].
[10] D. Neuffer and V. Shiltsev, JINST **13**, T10003 (2018), arXiv:1811.10694 [physics.acc-ph].
[11] V. V. Parkhomchuk and A. N. Skrinsky, Conf. Proc. C **830811**, 485 (1983).
[12] D. Neuffer, Part. Accel. **14**, 75 (1983).
[13] D. Neuffer, AIP Conf. Proc. **156**, 201 (1987).
[14] D. M. Kaplan (MAP, MICE), EPJ Web Conf. **95**, 03019 (2015), arXiv:1412.3487 [physics.acc-ph].
[15] D. Adey, R. Bayes, A. Bross, and P. Snopok, Ann. Rev.

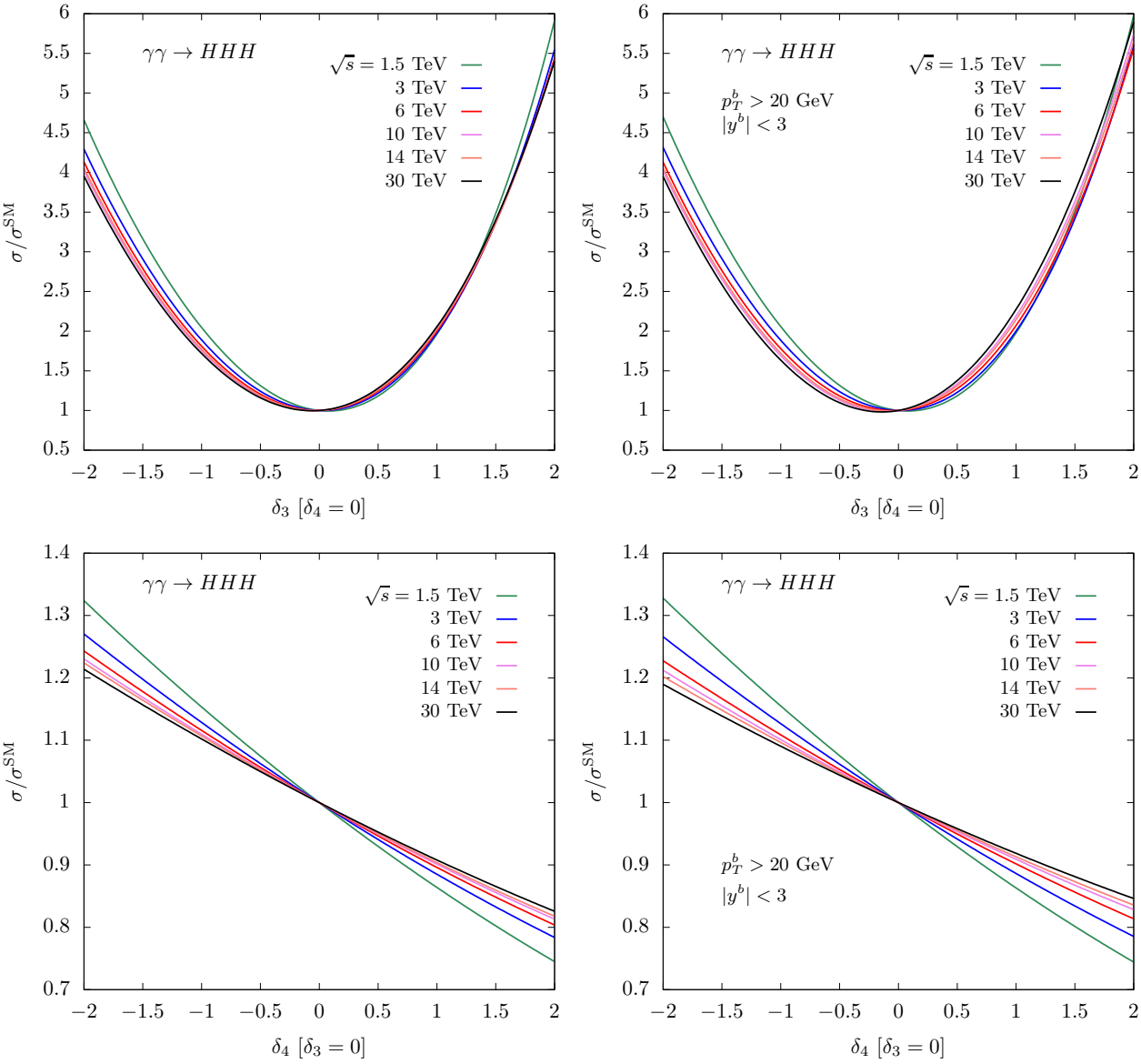

FIG. 15. Ratio of the integrated cross sections with and without anomalous Higgs self-couplings for the process $\gamma\gamma \to HHH$ in the inclusive setup (left plots) and after imposing acceptance cuts on the Higgs decay products (right plots) as a function of δ_3 (upper plots) and δ_4 (lower plots).

Nucl. Part. Sci. **65**, 145 (2015).

[16] M. Bogomilov *et al.* (MICE), Nature **578**, 53 (2020), arXiv:1907.08562 [physics.acc-ph].

[17] M. Bonesini (MICE), PoS **EPS-HEP2019**, 025 (2020).

[18] K. Long, D. Lucchesi, M. Palmer, N. Pastrone, D. Schulte, and V. Shiltsev, Nature Phys. **17**, 289 (2021), arXiv:2007.15684 [physics.acc-ph].

[19] A. R. Young and J. C. Nugent (MICE), PoS **EPS-HEP2019**, 021 (2020).

[20] D. Alesini *et al.*, "Positron driven muon source for a muon collider," arXiv:1905.05747 [physics.acc-ph].

[21] M. Antonelli, M. Boscolo, R. Di Nardo, and P. Raimondi, Nucl. Instrum. Meth. A **807**, 101 (2016), arXiv:1509.04454 [physics.acc-ph].

[22] M. Boscolo, M. Antonelli, O. R. Blanco-Garcia, S. Guiducci, S. Liuzzo, P. Raimondi, and F. Collamati, Phys. Rev. Accel. Beams **21**, 061005 (2018), arXiv:1803.06696 [physics.acc-ph].

[23] A. Costantini, F. De Lillo, F. Maltoni, L. Mantani, O. Mattelaer, R. Ruiz, and X. Zhao, JHEP **09**, 080 (2020), arXiv:2005.10289 [hep-ph].

[24] H. Al Ali *et al.*, "The Muon Smasher's Guide," (2021), arXiv:2103.14043 [hep-ph].

[25] R. Franceschini and M. Greco, Symmetry **13**, 851 (2021), arXiv:2104.05770 [hep-ph].

[26] E. Eichten and A. Martin, Phys. Lett. B **728**, 125 (2014), arXiv:1306.2609 [hep-ph].

[27] N. Chakrabarty, T. Han, Z. Liu, and B. Mukhopadhyaya, Phys. Rev. D **91**, 015008 (2015), arXiv:1408.5912 [hep-ph].

[28] D. Buttazzo, D. Redigolo, F. Sala, and A. Tesi, JHEP **11**, 144 (2018), arXiv:1807.04743 [hep-ph].

[29] P. Bandyopadhyay and A. Costantini, Phys. Rev. D **103**, 015025 (2021), arXiv:2010.02597 [hep-ph].

[30] T. Han, S. Li, S. Su, W. Su, and Y. Wu, "Heavy Higgs Bosons in 2HDM at a Muon Collider," (2021), arXiv:2102.08386 [hep-ph].

[31] W. Liu and K.-P. Xie, JHEP **04**, 015 (2021), arXiv:2101.10469 [hep-ph].

[32] T. Han, Z. Liu, L.-T. Wang, and X. Wang, Phys. Rev. D **103**, 075004 (2021), arXiv:2009.11287 [hep-ph].

[33] R. Capdevilla, F. Meloni, R. Simoniello, and J. Zurita, JHEP **06**, 133 (2021), arXiv:2102.11292 [hep-ph].

[34] S. Bottaro, A. Strumia, and N. Vignaroli, "Minimal Dark Matter bound states at future colliders," (2021), arXiv:2103.12766 [hep-ph].

[35] R. Capdevilla, D. Curtin, Y. Kahn, and G. Krnjaic, Phys. Rev. D **103**, 075028 (2021), arXiv:2006.16277 [hep-ph].

[36] D. Buttazzo and P. Paradisi, "Probing the muon g-2 anomaly at a Muon Collider," (2020), arXiv:2012.02769 [hep-ph].

[37] R. Capdevilla, D. Curtin, Y. Kahn, and G. Krnjaic, "A No-Lose Theorem for Discovering the New Physics of $(g-2)_\mu$ at Muon Colliders," (2021), arXiv:2101.10334 [hep-ph].

[38] N. Chen, B. Wang, and C.-Y. Yao, "The collider tests of a leptophilic scalar for the anomalous magnetic moments," (2021), arXiv:2102.05619 [hep-ph].

[39] W. Yin and M. Yamaguchi, "Muon $g-2$ at multi-TeV muon collider," (2020), arXiv:2012.03928 [hep-ph].

[40] G.-y. Huang, F. S. Queiroz, and W. Rodejohann, Phys. Rev. D **103**, 095005 (2021), arXiv:2101.04956 [hep-ph].

[41] G.-Y. Huang, S. Jana, F. S. Queiroz, and W. Rodejohann, "Probing the $R_{K^{(*)}}$ Anomaly at a Muon Collider," (2021), arXiv:2103.01617 [hep-ph].

[42] P. Asadi, R. Capdevilla, C. Cesarotti, and S. Homiller, "Searching for Leptoquarks at Future Muon Colliders," (2021), arXiv:2104.05720 [hep-ph].

[43] S. Bottaro, D. Buttazzo, M. Costa, R. Franceschini, P. Panci, D. Redigolo, and L. Vittorio, "Closing the window on WIMP Dark Matter," (2021), arXiv:2107.09688 [hep-ph].

[44] L. Di Luzio, R. Gröber, and G. Panico, JHEP **01**, 011 (2019), arXiv:1810.10993 [hep-ph].

[45] D. Buttazzo, R. Franceschini, and A. Wulzer, JHEP **05**, 219 (2021), arXiv:2012.11555 [hep-ph].

[46] PDFs effects in muon beams have been considered in [80, 81].

[47] T. Han, D. Liu, I. Low, and X. Wang, Phys. Rev. D **103**, 013002 (2021), arXiv:2008.12204 [hep-ph].

[48] T. Han, W. Kilian, N. Kreher, Y. Ma, J. Reuter, T. Striegl, and K. Xie, (2021), arXiv:2108.05362 [hep-ph].

[49] M. Chiesa, F. Maltoni, L. Mantani, B. Mele, F. Piccinini, and X. Zhao, JHEP **09**, 098 (2020), arXiv:2003.13628 [hep-ph].

[50] C. F. von Weizsacker, Z. Phys. **88**, 612 (1934).

[51] E. J. Williams, Phys. Rev. **45**, 729 (1934).

[52] Note that more conservative (smaller) luminosity values might be more realistic in the upper $\sqrt{s}$ range considered here (in particular for $\sqrt{s} \gtrsim 30$ TeV).

[53] J. Chen, T. Han, and B. Tweedie, JHEP **11**, 093 (2017), arXiv:1611.00788 [hep-ph].

[54] G. Altarelli, B. Mele, and F. Pitolli, Nucl. Phys. B **287**, 205 (1987).

[55] S. Actis, A. Denner, L. Hofer, A. Scharf, and S. Uccirati, JHEP **04**, 037 (2013), arXiv:1211.6316 [hep-ph].

[56] S. Actis, A. Denner, L. Hofer, J.-N. Lang, A. Scharf, and S. Uccirati, Comput. Phys. Commun. **214**, 140 (2017), arXiv:1605.01090 [hep-ph].

[57] A. Denner, J.-N. Lang, and S. Uccirati, JHEP **07**, 087 (2017), arXiv:1705.06053 [hep-ph].

[58] A. Denner, J.-N. Lang, and S. Uccirati, Comput. Phys. Commun. **224**, 346 (2018), arXiv:1711.07388 [hep-ph].

[59] A. Denner and S. Dittmaier, Nucl. Phys. B **844**, 199 (2011), arXiv:1005.2076 [hep-ph].

[60] A. Denner and S. Dittmaier, Nucl. Phys. B **658**, 175 (2003), arXiv:hep-ph/0212259.

[61] A. Denner and S. Dittmaier, Nucl. Phys. B **734**, 62 (2006), arXiv:hep-ph/0509141.

[62] A. Denner, S. Dittmaier, and L. Hofer, Comput. Phys. Commun. **212**, 220 (2017), arXiv:1604.06792 [hep-ph].

[63] M. Chiesa, C. Oleari, and E. Re, Eur. Phys. J. C **80**, 849 (2020), arXiv:2005.12146 [hep-ph].

[64] M. Chiesa, A. Denner, and J.-N. Lang, Eur. Phys. J. C **78**, 467 (2018), arXiv:1804.01477 [hep-ph].

[65] W. Kilian, T. Ohl, and J. Reuter, Eur. Phys. J. C **71**, 1742 (2011), arXiv:0708.4233 [hep-ph].

[66] M. Moretti, T. Ohl, and J. Reuter, "O'Mega: An Optimizing matrix element generator," (2001), arXiv:hep-ph/0102195.

[67] A. Denner, S. Dittmaier, M. Roth, and D. Wackeroth, Nucl. Phys. B **560**, 33 (1999), arXiv:hep-ph/9904472.

[68] A. Denner, S. Dittmaier, M. Roth, and L. H. Wieders, Nucl. Phys. B **724**, 247 (2005), [Erratum: Nucl.Phys.B 854, 504–507 (2012)], arXiv:hep-ph/0505042.

[69] A. Denner and S. Dittmaier, Nucl. Phys. B Proc. Suppl. **160**, 22 (2006), arXiv:hep-ph/0605312.

[70] M. A. C. Cummings, S. Kahn, A. Morris, D. Hedin, and J. Kozminski, Conf. Proc. C **110328**, 2297 (2011).

[71] S. A. Kahn, M. A. C. Cummings, T. J. Roberts, A. O. Morris, D. Hedin, and J. Kozminski, Conf. Proc. C **110328**, 2300 (2011).

[72] N. V. Mokhov and S. I. Striganov, Phys. Procedia **37**, 2015 (2012), arXiv:1204.6721 [physics.ins-det].

[73] N. V. Mokhov, S. I. Striganov, and I. S. Tropin, in *5th International Particle Accelerator Conference* (2014) arXiv:1409.1939 [physics.ins-det].

[74] V. Di Benedetto, C. Gatto, A. Mazzacane, N. V. Mokhov, S. I. Striganov, and N. K. Terentiev, JINST **13**, P09004 (2018), arXiv:1807.00074 [physics.ins-det].

[75] N. Bartosik *et al.*, "Preliminary Report on the Study of Beam-Induced Background Effects at a Muon Collider," (2019), arXiv:1905.03725 [hep-ex].

[76] N. Bartosik *et al.*, JINST **15**, P05001 (2020), arXiv:2001.04431 [hep-ex].

[77] D. Lucchesi *et al.*, PoS **EPS-HEP2019**, 118 (2020).

[78] D. d'Enterria, P. Rebello Teles, and D. E. Martins, in *17th conference on Elastic and Diffractive Scattering* (2017) arXiv:1712.07023 [hep-ph].

[79] A. Abada *et al.* (FCC), Eur. Phys. J. C **79**, 474 (2019).

[80] T. Han, Y. Ma, and K. Xie, Phys. Rev. D **103**, L031301 (2021), arXiv:2007.14300 [hep-ph].

[81] T. Han, Y. Ma, and K. Xie, "Quark and Gluon Contents of a Lepton at High Energies," (2021), arXiv:2103.09844 [hep-ph].